ChemPubSoc Europe

DOI: 10.1002/chem.201602578

CHEMISTRY A European Journal Full Paper

Nanostructures |*Hot Paper*|

Full Solution-Processed Synthesis and Mechanisms of a Recyclable and Bifunctional Au/ZnO Plasmonic Platform for Enhanced UV/Vis Photocatalysis and Optical Properties

Da-Ren Hang,*[a] Sk Emdadul Islam,[a] Chun-Hu Chen,[b] and Krishna Hari Sharma[a]

Abstract: The synthesis of noble metal/semiconductor hybrid nanostructures for enhanced catalytic or superior optical properties has attracted a lot of attention in recent years. In this study, a facile and all-solution-processed synthetic route was employed to demonstrate an Au/ZnO platform with plasmonic-enhanced UV/Vis catalytic properties while retaining strengthened luminescent properties. The visible-light response of photocatalysis is supported by localized surface plasmon resonance (LSPR) excitations while the enhanced performance under UV is aided by charge separation and strong absorption. The enhancement in optical properties is mainly due to local field enhancement effect and coupling between exciton and LSPR. Luminescent characteristics are investigated and discussed in detail. Recyclability tests showed that the Au/ZnO substrate is reusable by cleaning and has a long shelf life. Our result suggests that plasmonic enhancement of photocatalytic performance is not necessarily a trade-off for enhanced near-band-edge emission in Au/ZnO. This approach may give rise to a new class of versatile platforms for use in novel multifunctional and integrated devices.

Introduction

Photocatalytic degradation of hazardous materials in water, such as dyes and toxic organic pollutants, is a promising method for environmental protection. A lot of attention has been drawn to semiconductor nanomaterials as photocatalysts, which generally benefit from large surface area, high optical sensitivity, and varied morphologies. Following optical absorption of semiconductor photocatalysts, photogenerated electrons migrate to the surface to initiate the reduction process while the holes in the valence band move to the surface to induce the oxidation process. Among nanostructured semiconductor photocatalysts, TiO_2 and ZnO are well-known in the field of UV-light-driven photocatalysis.[1,2] ZnO is a versatile wide-band-gap II-VI semiconductor with wurtzite crystal structure. A direct gap of 3.37 eV and large exciton binding energy (60 meV) makes it one of the most promising materials for light-emitting devices, sensing, and nanostructure devices.[3,4,5] Superhydrophobic surfaces of ZnO have been recently demonstrated.[6] By sharing similar photocatalytic mechanisms with more popular TiO_2, ZnO also shows huge potential in the photodegradation of environmental pollutants and photoelectrochemical water splitting.[7,8] In addition, a few reports have shown that ZnO has a higher efficiency than TiO_2 in the photocatalytic degradation of some organic molecules.[9,10]

One major drawback for ZnO as a photocatalyst is the low solar energy conversion efficiency. Because of the short wavelength cutoff of ZnO absorption, it can only convert a rather small portion ($\approx$5%) of the solar radiation into chemical energy. Several attempts have been utilized to extend the absorption range of ZnO to the visible-light region. The use of a hybrid nanomaterial is by far the most effective strategy. One way is to couple ZnO with a narrow band-gap semiconductor with favorable energy band alignment for efficient visible photon absorption and charge carrier separation.[11,12] The other way is to employ a noble metal/semiconductor composite as a plasmonic photocatalyst.[13–16] Recently, modification of the photoelectric conversion properties by a localized surface plasmon resonance (LSPR) effect has been under intensive investigation. LSPR arises as collective oscillations of the free conduction-band electrons at the interface between noble metal nanoparticles (NPs) and semiconductor which are resonant with the electromagnetic field of incident light in the visible and IR regions. The resonance results in electric field amplification both inside and in the near-field zone outside the metal nanoparticles. The resonance frequency of LSPs depends on many factors, such as shapes and sizes of noble metal NPs, metal coverage, and the coated dielectric layers. Three advantageous factors are mainly considered in plasmonic-enhanced photocatalysis: 1) increasing electron-hole separation by the charge-transfer process, 2) extension of light absorption, and

[a] *Prof. D.-R. Hang, S. E. Islam, K. H. Sharma*
Department of Materials and Optoelectronic Science
National Sun Yat-sen University, 70 Lienhai Rd.
Kaohsiung 80424 (Taiwan)
E-mail: drhang@faculty.nsysu.edu.tw

[b] *Prof. C.-H. Chen*
Department of Chemistry, National Sun Yat-sen University
70 Lienhai Rd., Kaohsiung 80424 (Taiwan)

Supporting information for this article can be found under http://dx.doi.org/10.1002/chem.201602578.

3) LSPR-induced charge carrier excitation followed by carrier migration to the semiconductor.

Furthermore, noble metal/semiconductor composite is also known for its functionality to modify the emission properties of a semiconductor. Several metal NPs have been decorated on ZnO to study the LSP effect on photoluminescence (PL) properties, such as Au/ZnO,[17–20] Ag/ZnO,[21] Pt/ZnO,[22] and Al/ZnO.[23] The PL properties of Au/ZnO hybrid structures varies in published reports. Many authors found that the LSP effect is positive to the ZnO emission property in which near-band-edge (NBE) emission is enhanced and defect emission (DE) is suppressed.[17–20] Inversely, a few studies have reported that both NBE and DE emissions were suppressed.[13–16,24,25] Recently, Viter et al. showed that PL response to Au decoration is very sensitive to the composition and the structure so that selective enhancement may be possible.[26] By tuning Au thickness using sputtering, they can change the PL properties from enhanced NBE with suppressed DE to the reverse behavior—reduced NBE emission with enhanced DE. A multilayer model was proposed to account for their observation. Given the fact that controversial results exist, the complicate mechanisms of the LSP effect to the emission of Au/ZnO composite is still not well-understood.

In plasmonic-enhanced photocatalytic experiments, the decrease of PL intensity is generally observed, which can be attributed to the increased spatial separation of photogenerated electron-hole pairs. Thereby, it appears to be a great challenge to construct and realize one nanostructured Au/ZnO substrate with both enhanced photocatalytic efficiency and favorably enhanced NBE PL emission. In this paper, we report on a simple synthetic route to realize a plasmonic-enhanced Au/ZnO nanocomposite platform that can be renewable after multiple usage. Unlike many reported cases in which enhanced photocatalytic performance cannot coexist with enhanced NBE emission, both enhancement due to LSP is shown in this study. Highly enhanced photocatalytic activity compared to pristine ZnO is demonstrated in the degradation of methylene blue (MB) under UV and visible-light illumination. Moreover, respective mechanisms for the performance enhancement were studied and proposed. Our work provides a clue for a new opportunity in the construction of recyclable and plasmonic-enhanced multifunctional devices with a cost-effective synthesis route.

Results and Discussion

Characterization of pristine ZnO NRs and Au/ZnO hybrids

The morphology of pristine ZnO NRs and Au/ZnO NRs arrays were revealed by SEM measurements. Typical SEM images of pristine ZnO NRs arrays at low magnification are presented in Figure 1a. As can be seen, a high density of vertically aligned ZnO NRs were grown on the substrate. Figure 1b shows the high-resolution SEM image, in which the hexagonal NRs are suggestive for the preferred growth direction of the *c*-axis of wurtzite ZnO. The diameters of pristine ZnO NRs are in the range of 90–140 nm and the average length of the NRs is about 500 nm. For the photosynthesis of the Au nanostructure, the as-prepared ZnO NRs substrate was further immersed into the aqueous solution of $HAuCl_4$ under irradiation of a UV lamp for the reduction of Au NPs on the side walls of the ZnO NR surface. Figure 1c shows the SEM image of the Au/ZnO NRs. As indicated by the square in Figure 1c, Au NPs were attached on the ZnO NRs surfaces. The size of the Au NPs is around 80 to 100 nm. It is worth noting that the Au NPs are composed of few small-sized dots with an average diameter of 8 nm. The Au nanoparticles are not distributed uniformly on the ZnO surfaces. It suggests that the nucleation of small-sized Au dots is site-selective in the photoreduction process. The formation of our Au/ZnO heterostructure is discussed by the following reactions:[13]

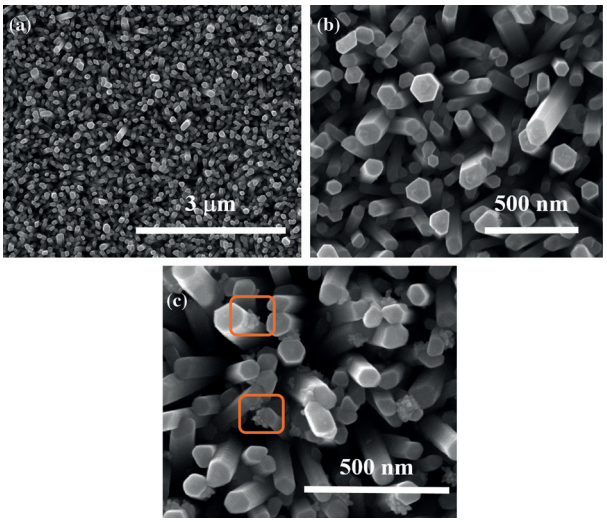

Figure 1. SEM images of pristine ZnO nanorod arrays shown in a) large-scale overview and b) high-magnification. c) High-resolution SEM image of Au/ZnO nanorod arrays.

$$ZnO + h\nu \rightarrow ZnO\ (e^-, h^+) \quad (1)$$

$$AuCl_4^- + 3\,e^- \rightarrow Au + 4\,Cl^- \quad (2)$$

As UV light excites ZnO, some electrons are delocalized and subsequently migrate to the surface of ZnO NRs, as shown in Equation (1). These photogenerated electrons can reduce the adsorbed Au^{3+} to Au^0, as expressed in Equation (2). Once the initial nucleation sites of Au nanocrystals are activated on the surface of the ZnO NRs, the subsequent reduction of Au^{3+} would preferably occur at the pre-existing nucleation sites and then result in the formation of dot ensemble nanostructures. The crystalline structure and phase purity of the samples were examined by the XRD measurement, as shown in Figure 2a. The intense peaks at $2\theta = 34.48^\circ$ for both samples are attributed to the (002) plane of the ZnO NRs, stating that the ZnO NRs are vertically aligned to the substrate. No other peaks are detected in both patterns, further indicating their high phase purity. However, the diffraction peak of the Au nanocrystal was not detected for the Au/ZnO nanohybrid. It can be due to the minute amount of Au NPs deposited on the ZnO NRs surface.

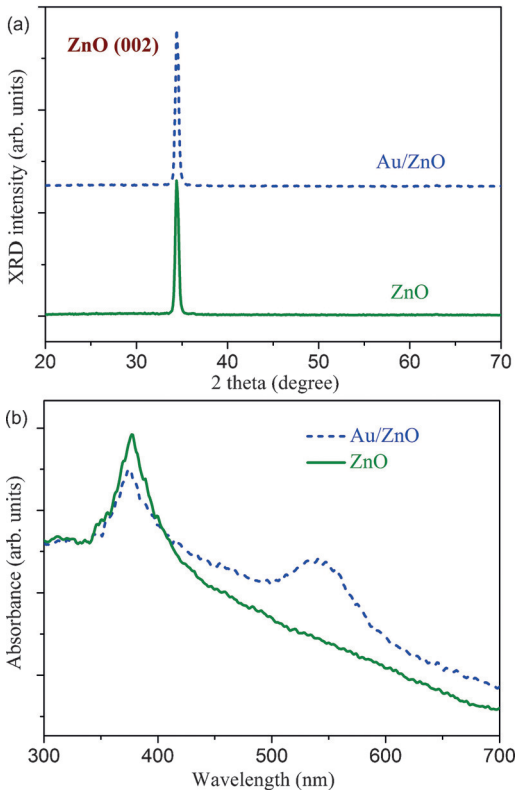

Figure 2. a) XRD θ–2θ scans for pristine ZnO NRs and Au/ZnO nanohybrid. b) UV/Vis absorption spectra of ZnO NRs and Au/ZnO.

To test this, we prepared another Au/ZnO NR sample by adopting higher Au precursor concentration (10^{-3} M) solution during photodeposition. In this case, a sharp peak at 38.1^0 of the XRD pattern can be revealed, which corresponds to the (111) plane of the gold nanostructures, as shown in Figure S1 in the Supporting Information.

In order to provide supplementary insight into Au NPs in the hybrid sample, we proceeded to carry out XPS measurements, in which C 1s (284.8 eV) was used to calibrate the binding energies. By surveying the surface composition of these substrates, changes to chemical states on the surface of ZnO after Au deposition can be detected. Figure 3a displays the full XPS spectra which reveal the existence of Zn, O, and C elements for pristine ZnO NR and the expected presence of Zn, O, Au, and C elements for Au/ZnO. No other impurity species is detected for Au/ZnO nanohybrids. High-resolution XPS spectra for Zn 2p are presented in Figure 3b. For pristine ZnO and Au/ZnO nanohybrid, there is no shift to the binding energy peaks of Zn $2p_{3/2}$ and Zn $2p_{1/2}$ that locate at 1021.8 and 1044.8 eV, respectively. The energy separation between the two peaks is 23.0 eV, which confirms that the Zn species exists mainly in the Zn^{2+} chemical state in both the ZnO NRs and Au/ZnO nanocomposite.[27] The O 1s binding energies of Au/ZnO are highlighted in Figure 3c, which shows an asymmetric profile. It can be fitted to two symmetrical peaks, indicating two different kinds of O species in the sample. The main peak located at around 531.6 eV is ascribed to the lattice oxygen of ZnO. Another contribution peaks at about 532.8 eV and is attributed to the formation of zinc hydroxide with chemisorbed

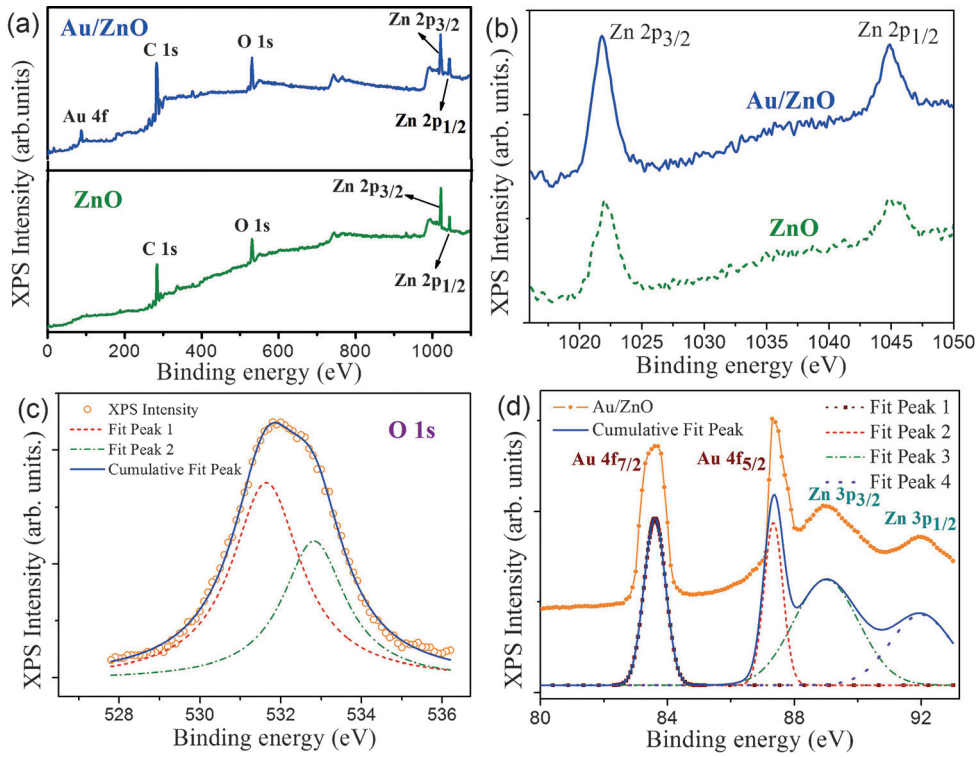

Figure 3. XPS core level spectra of our samples showing a) full XPS spectra and binding energies of b) Zn 2p, c) O1s, and d) Zn 3p and Au 4f electrons.

oxygen species.[28] Figure 3d shows the core-level binding energies of Zn 3p and Au 4f electrons of Au/ZnO composite, which can be further fitted to four peaks. The two sharp peaks centered at 83.6 and 87.3 eV can be attributed to Au $4f_{7/2}$ and Au $4f_{5/2}$, respectively. The binding energy of Au 4f exhibits a redshift of 0.4 eV, compared with those of bulk gold values ($4f_{7/2}$, 84.00 eV and $4f_{5/2}$, 87.71 eV).[29] The negative binding energy shift of the Au/ZnO composite evidences an electronic interaction between the Au and ZnO NR surface, in which electrons can be transferred from Au NPs to the underlying ZnO support due to the work function difference between ZnO and Au.[30,31,32] Two more peaks in the high-energy side originated from the binding energy of Zn $3p_{3/2}$ and Zn $3p_{1/2}$, which are located at 88.9 and 91.9 eV, respectively. Thus, we can conclude that XPS analysis clearly confirms the realization of the Au NPs on the ZnO NRs surface, which is consistent with the SEM results. The light-absorption properties of pristine ZnO NRs and Au/ZnO heteroarrays in the UV/Vis region are presented in Figure 2b. In the absorption spectrum of the pristine ZnO sample, the dominating peak at 374 nm originates from the band-edge absorption of ZnO NRs. In the case of Au/ZnO, there appears an additional peak at 542 nm, which is due to the surface plasmon absorption of Au NPs. The characteristic LSPR band provides another proof for surface Au NPs attached on ZnO NRs and should further facilitate light harvesting in the visible range.

Photocatalytic activities of Au/ZnO NRs

The photocatalytic degradation of MB is adopted as an exemplary reaction to evaluate the photocatalytic capabilities of our catalysts. Under UV or visible-light irradiation, the changes in the characteristic absorption peak of MB at 663 nm were used to monitor the photocatalytic degradation process. The general principle of photocatalysis via ZnO NRs is based on the photoinduced generation of electron-hole pairs, which react with both oxygen and water molecules to yield strongly oxidizing radical species, which in turn promote the oxidation of organic dyes.[33] Figure 4a presents the blank test results under two different conditions: 1) in the presence of Au/ZnO photocatalysts but in the dark, and 2) with visible-light illumination but in the absence of the photocatalysts. For both cases, no meaningful amount of MB degradation after 2 h is found, signifying self-sensitized photolysis can be neglected. First we present the results obtained under UV-light illumination. The time-dependent absorption spectra of MB solutions in the presence of ZnO and Au/ZnO substrates are displayed in Figure 4b and c, respectively. Under UV-light illumination, photogenerated carriers in ZnO trigger the degradation of MB dyes, as shown in Figure 4b. Exceptionally enhanced photocatalytic activity has been found in the presence of Au/ZnO catalyst, almost 91% degradation of MB dye is attained after 2 h irradiation, as presented in Figure 4c. It indicates that the degradation efficiency can be enhanced by inclusion of Au NPs for the ZnO catalyst under this condition. Next, we present the results obtained under visible-light illumination. As presented in Figure S2, Supporting Information a negligible amount of MB degradation

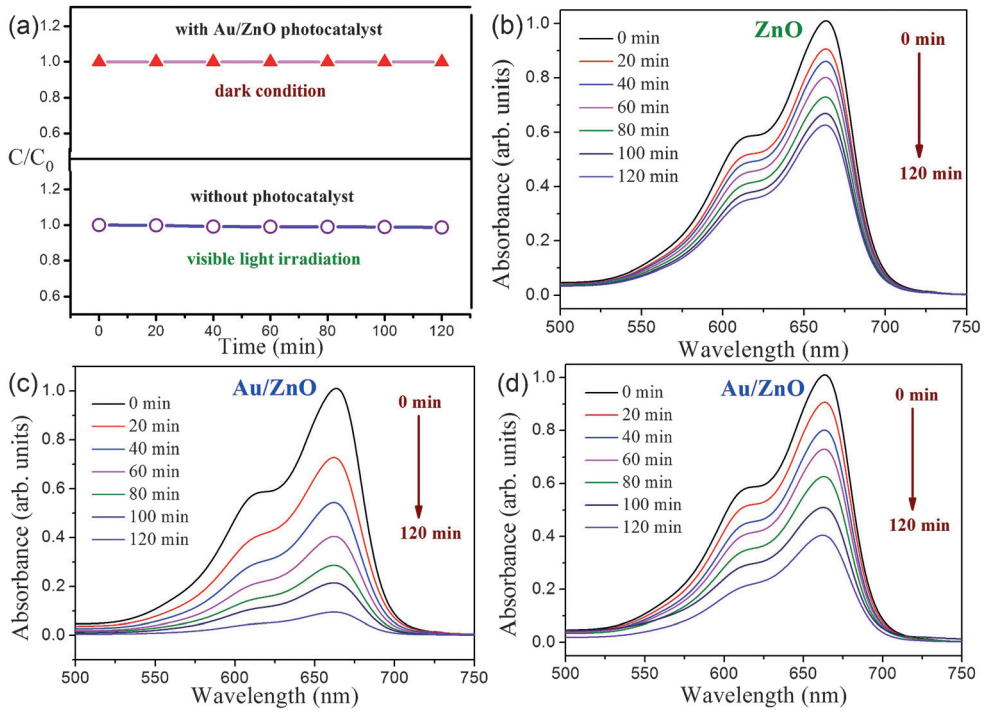

Figure 4. a) Blank tests for the photodegradation of MB. UV-light-driven photodegradation of MB in the presence of b) pristine ZnO NRs and c) Au/ZnO. d) Time-dependent absorption spectra of MB under visible light in the presence of Au/ZnO.

can be seen in the case of pristine ZnO NRs in 2 h. Figure 4d exhibits the time-dependent absorption spectra of MB solution in the presence of Au/ZnO substrate under visible light. We found that MB decomposed progressively with the increase of irradiation time by means of Au/ZnO catalyst (60% in 2 h), as shown in Figure 4d. Therefore, under visible-light illumination, the deposition of Au NPs on the ZnO NR surface can significantly raise the decomposition rate of dye as compared to pristine ZnO NRs substrate.

To quantitatively compare the photocatalytic capabilities, degradation curves of the pristine ZnO NRs and Au/ZnO substrates under UV and visible illumination are presented in Figure 5a and 5b, respectively. Here C_0 and C correspond to the initial and modified concentrations of MB, respectively. MB concentration nearly quenches in the presence of hybrid catalyst, as shown in Figure 5a. Several factors contribute to the superior photocatalytic efficiency under UV-light illumination. Charge separation of photogenerated electrons and holes plays a significant role in the substantial enhancement of photocatalytic efficiency, which is further discussed in the next section. As shown in Figure 5b, it is found that with the incorporation of Au NPs, the degradation of MB under visible irradiation also drastically increased from 2.9 to 60% in the period of 2 h. In the context of the Langmuir–Hinshelwood first-order kinetics model, the degradation rate r can be expressed as $r = dC/dt = \kappa KC/(1+KC)$, in which C is the concentration of MB at time t, κ is the reaction rate constant, and K is the adsorption coefficient of the reactant. When the initial concentration is very low (as in this experiment, $C_0 = 10\ mg\ L^{-1}$ for MB), this equation can be simplified to an apparent first-order model:[34]

$$\ln(C_0/C) = \kappa Kt = kt \quad (3)$$

in which k is the apparent first-order rate constant (min^{-1}). Figure 5c shows the $-\ln(C_0/C)$ versus time curves under both experimental conditions, in which all the data can be fitted well into linear curves, indicating that it follows the first-order reaction kinetic model. Under UV irradiation, the apparent first-order rate constant increases from 0.0038 to 0.018 min^{-1} by loading Au NPs on the ZnO NRs. It represents a ≈470% increase in degradation rate, compared to the pristine ZnO NRs. Secondly, the degradation rate constant increases remarkably from 0.0002 to 0.0074 min^{-1} by Au loading under the visible-light irradiation setup. The degradation under visible illumination is activated by the hybrid photocatalyst. It clearly demonstrates that these Au NPs enable ZnO NRs to be visible-light responsive in photocatalysis.

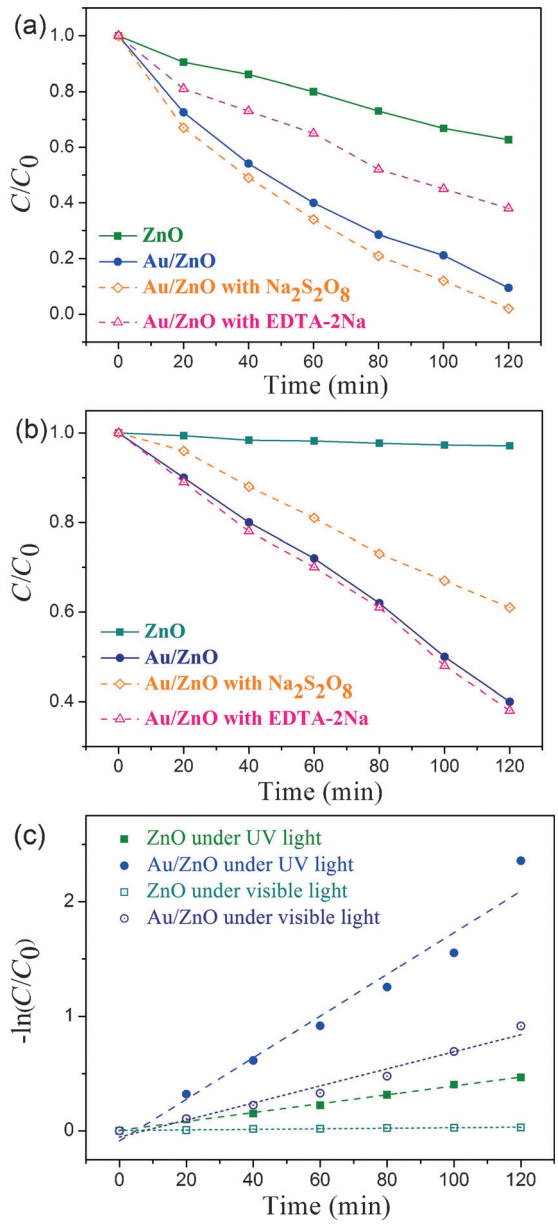

Figure 5. Photodegradation kinetics of MB using pristine ZnO NRs and Au/ZnO under a) UV and b) visible light. Effects of scavengers on respective photodegradation performance are shown by open symbols. c) The plot of $-\ln(C_0/C)$ versus irradiation time.

Photocatalytic degradation mechanism

The origin of superior photocatalytic performance of Au/ZnO over pristine ZnO NRs can be understood comprehensively by the proposed mechanisms schematically presented in Scheme 1. To describe the photocatalytic processes, the following advocated reactions are responsible for the degradation of MB dye under UV and visible-light irradiation.

$$e^- + O_2 \rightarrow O_2^{\bullet -} \quad (4)$$

$$O_2^{\bullet -} + 2H^+ \rightarrow 2OH^{\bullet} \quad (5)$$

$$h^+ + OH^- \rightarrow OH^{\bullet} \quad (6)$$

$$O_2^{\bullet -} \text{ or } OH^{\bullet} + \text{dye (MB)} \rightarrow \text{degraded products} \quad (7)$$

Due to the work function difference (5.1 eV for Au and 5.2 eV for ZnO), electrons transfer from Au NPs to the ZnO side, resulting in an Ohmic-type junction after the metal-semiconductor composite reaches equilibrium, as shown in Scheme 1a.[35] Upon UV-light excitation, electron and hole pairs

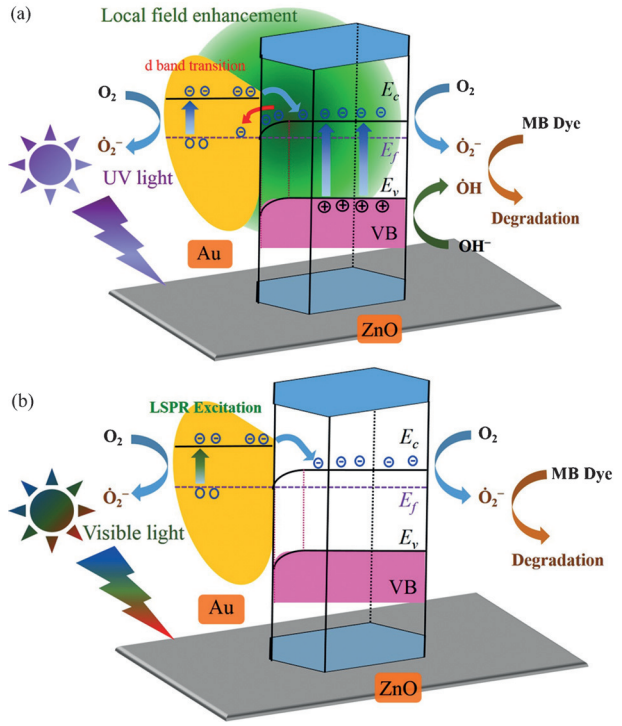

Scheme 1. Schematic illustrations of the mechanism of enhanced photocatalysis for the Au/ZnO under irradiation of a) UV light and b) visible light. In the presentation, the metal-semiconductor junction is drawn to coincide with one edge of ZnO NR in real-space geometry.

are generated in ZnO, as depicted by the reaction in Equation (1). The photoexcited electrons in the conduction band of ZnO are easily driven by the static electric field in the junction to the Au NPs, which facilitates charge separation of electron and hole pairs. As indicated by the reactions in Equations (4) and (5), the electrons transferred to the Au NPs and remaining ones on the ZnO NR surface capably react with dissolved oxygen to produce superoxide radical anions ($O_2^{\bullet-}$) and consecutively those anions react with H_2O to form hydroxyl ($OH^{\bullet}$) radicals. In addition, the photogenerated holes can diffuse to the surface of ZnO and react with an OH^- ion or water molecule adhering to the NR surface to produce reactive hydroxyl radicals, as in the reaction in Equation (6). These radical anions ($O_2^{\bullet-}$) and reactive ($OH^{\bullet}$) radicals are highly active for oxidation and dissociation of MB dye, as shown in the reaction in Equation (7).

As the wavelength of irradiated UV light is larger than the size of the Au NPs, the high-density electrons in Au NPs formed an oscillating electron cloud. The hot spots on the NPs produce a strong local electric field that can greatly enhance the carrier generation in ZnO. Close to the junction, these carriers are prevented from recombination and participate in the photocatalytic reactions. In addition, a large number of electrons in the Au NPs can be pumped from the 5d to 6sp band by UV light. They could react with adsorbed O_2 molecules directly or transfer to the conduction band of ZnO and then being swept back to Au NPs by the intrinsic electric field, as depicted in Scheme 1a. Therefore, a significantly higher number of active charged carriers can be available in the Au/ZnO substrate for photocatalytic reactions, contributing to the drastic enhancement of photodegradation efficiency. Scheme 1b illustrates the processes under visible-light irradiation. While carrier generation is negligible in ZnO NRs, the electrons in the Au NPs can be promoted to the excited LSPR states. These energetic electrons favorably transfer to the conduction band of ZnO and successively participate in photocatalytic reactions there. In this situation, electrons transferring to the ZnO side and O_2 molecules adsorbed on the surface of ZnO NRs mainly contribute to photocatalytic processes. As a result, the electron is the sole reactive species and the photodegradation rate is slower than the corresponding rate under UV-light irradiation.

To have a deeper insight into the active species involved during the degradation of MB in the presence of Au/ZnO nanocomposite, the reaction of dye solution was further accompanied with scavengers. Sodium persulfate ($Na_2S_2O_8$) and ethylenediaminetetraacetic acid disodium salt (EDTA·2Na) were used as the electron and hole scavengers, respectively. The results of degradation under UV light are shown by open symbols in Figure 5a. It was observed that MB decomposes more rapidly after electron sacrificial agents were added to the dye solution. Contrariwise, we found a substantial inhibition of degradation efficiency in the presence of hole scavenger, suggesting the important role of the hole in the degradation process of MB. The enhancement of photodegration by the addition of electron capture agents is attributed to the boosted separation of photoexcited electron and hole pairs. As the photogenerated electrons on the semiconductor surface are taken by electron capture agents, the carrier recombination is suppressed and the holes have more time to oxidize the H_2O to form the strong reactive $OH^{\bullet}$. As a consequence, holes play a vital role in decomposing MB under UV light. Next the results under visible light are presented by open symbols in in Figure 5b. It shows that adding a hole scavenger has little influence on the degradation efficiency of MB yet the degradation process of MB was largely repressed by the addition of electron-capture agents in this case. Thus the electron is the main responsive species under visible irradiation, rather than holes. Overall, our scavenger test results are in support of the proposed mechanisms above. Herein, we can conclude that the presence of Au NPs makes the hybrid structure undergo a visible-light-driven photocatalysis and further enhances the photodegradation efficiency under UV irradiation.

The optical properties of Au/ZnO NRs

To explore light-scattering properties of the pristine and the plasmonic ZnO NR arrays, Raman measurement was conducted at room temperature. As shown in Figure 6a, the dominant peaks in both Raman spectra at 430 cm^{-1} correspond to the nonpolar $E_2^{(high)}$ mode of ZnO, which is mainly attributed to the vibration of the oxygen atoms in the wurtzite lattice.[36] The second peak occurring at around 582 cm^{-1} is due to A_1(LO)/E_1(LO) modes of ZnO.[36,37] The E_1 (LO) mode is mainly ascribed to the defect formation of oxygen vacancies (V_O). The presence

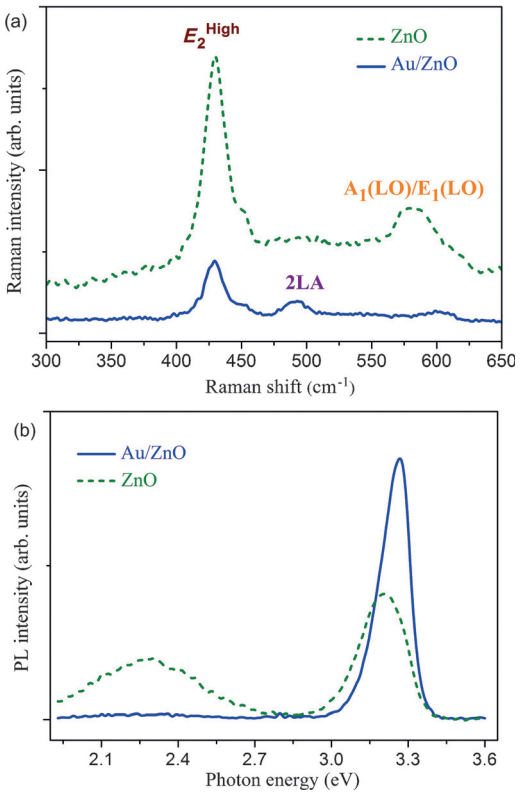

Figure 6. a) Raman spectra of pristine ZnO NRs and Au/ZnO at room temperature. b) Room temperature PL spectra of pristine ZnO NRs and Au/ZnO.

of the E_1 (LO) mode is indicative of a host defect related to an oxygen vacancy in the pristine substrate.[38–40] The two peaks for Au/ZnO are relatively weaker than the corresponding ones for pristine ZnO and there is also a new broad peak appearing at around 490 cm^{-1}. The suppressed E_1(LO) mode may be due to the fact that Au tends to nucleate on V_O and passivates the defects on the surfaces.[14,30] The new peak appearing around 490 cm^{-1} is attributed to the 2LA mode, which is a second-order scattering effect aided by multiphonon processes.[41,42] It is too weak to be detected in the pristine ZnO substrate. The enhancement of this Raman mode may be credited to the local-field enhancement due to LSPR of the Au NPs on the ZnO surface. An analogous result was recently reported for the case of Ag/ZnO heterostructures.[43] Thus significant plasmonic effects of Au NPs are found, which also suggests that deposited Au NPs strongly bonded with ZnO surfaces in Au/ZnO.

Figure 6b presents the full RT PL spectra. For pristine ZnO, the UV emission at 3.2 eV is the characteristic NBE emission arising mostly from the recombination of free photogenerated electrons and holes. In addition, there is a broad visible DE with slightly weaker intensity which is associated with oxygen vacancies or other vacancy-related defects. On the other hand, the Au/ZnO sample exhibits an evidently stronger NBE emission band which is slightly blueshifted to 3.26 eV. The visible DE is completely suppressed in this hybrid sample, which indicates that the sample is also favorable for photonics applications.

Our result is in sharp contrast to many photocatalytic reports in which a decrease of PL intensity is generally observed. To account for our results, relevant mechanisms are illustrated in the energy band diagrams in Scheme 2. Before metal NP/semiconductor junction formation, the Fermi energy level of ZnO is lower than that of Au, as shown in Scheme 2a. The defect energy levels responsible for DE are denoted by the continuous defect band. When the Au NPs are loaded on the ZnO NRs, electron transfer from Au NPs to ZnO NRs occurs until they attain a new equilibrium and share a joint Fermi level, as depicted in Scheme 2b. Scheme 2c displays several physical processes as a UV laser irradiates on the Au/ZnO sample. Two mechanisms, the local field enhancement and the charge-transfer model, are responsible for the plasmonic-enhanced NBE enhancement.[17,44] Under the excitation of 325 nm laser, a high-density electron cloud in NPs collectively oscillates with the incoming electromagnetic field, yielding a stronger local field than the incident light field.[45,46] The augmented energy density of optical excitation leads to an enhanced excitation rate and a larger quantity of photogenerated electrons in the conduction band, yielding an enhancement in the NBE intensity. Accompanied by the accumulation of electrons close to the junction, as shown in Scheme 2c, the Fermi level of the ZnO floats up slightly, bringing about a small blueshift in the NBE emission. Furthermore, a closer inspection of Figure 1c suggests that many NPs have clear edges instead of being smoothly round. Noble-metal NPs with sharp edges have been recently found to be very efficient hot spots that generate a giant local electric field.[47] This picture is also consistent with the observation of the weak second-order Raman mode in Figure 6a, further highlighting the strong interaction of Au NPs and ZnO NRs. Next, as shown by the energy-level alignment, the defect band in ZnO matches well with the Fermi level of Au, which can be inferred by the DE in Figure 6b. The electrons in the defect band in ZnO can transfer to the Fermi level of Au, and thereby increase the resonant electron density in Au NPs. Alternatively, DE from few electrons in the defect band can be absorbed resonantly to promote the electrons in Au NPs to excited LSPR states. These energetic electrons can relax nonradiatively by transferring back to the conduction band of ZnO, yielding an increased density of electrons in the conduction band of ZnO, as shown in Scheme 2c. Thus the DE can be effectively suppressed by the coupling between defect states and LSP states.

A low-temperature PL measurement has been carried out on these samples to investigate more excitonic properties. Figure 7a compares the NBE PL spectra of pristine ZnO NRs and the Au/ZnO samples recorded at 10 K. As expected, the Au NPs decorated sample shows excellent enhanced PL emission. The enhancement ratio of PL intensity at 10 K is 4.5, significantly higher than the ratio 1.46 taken at 300 K, as previously shown in Figure 6b. The sharp increase of the PL enhancement ratio at low temperatures, according to previous studies, can be attributed to two factors regarding plasmon coupling.[48,49] The first one is the increase of plasmonic density of states and the second one is the reduced plasmon damping resulting from electron–phonon interactions. At 10 K, the dominant

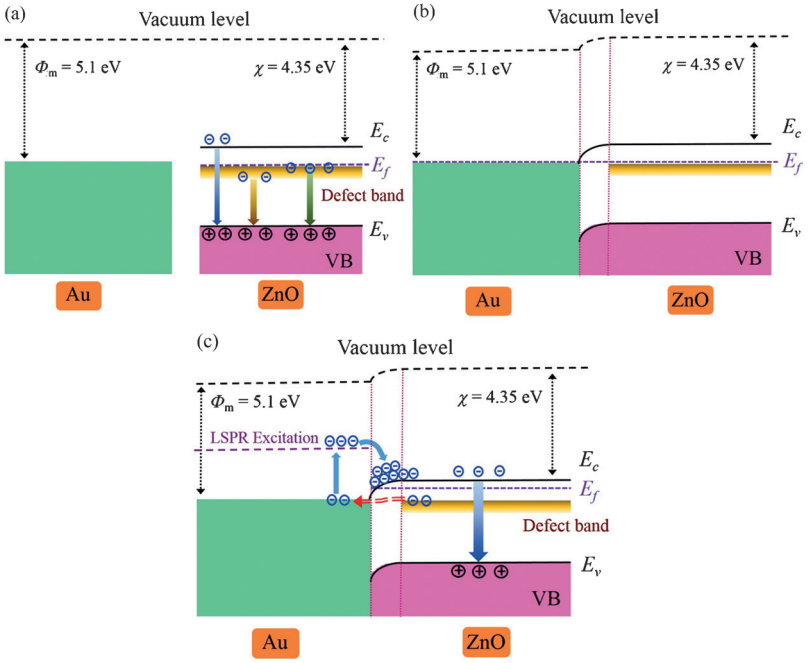

Scheme 2. Schematic representation of the energy band alignment of Au/ZnO and the enhancement mechanism of PL. a) The respective energy band structure of Au metal and ZnO. Visible DE of ZnO is due to the transition from the defect band. Here, Φ_m is the work function of Au and χ is the electron affinity of ZnO. b) The energy band alignment of Au/ZnO after junction formation, in which a uniform Fermi level emerges. c) Upon irradiation of 325 nm laser, the DE is suppressed by electrons transfer to the conduction band of ZnO through LSPR excitation.

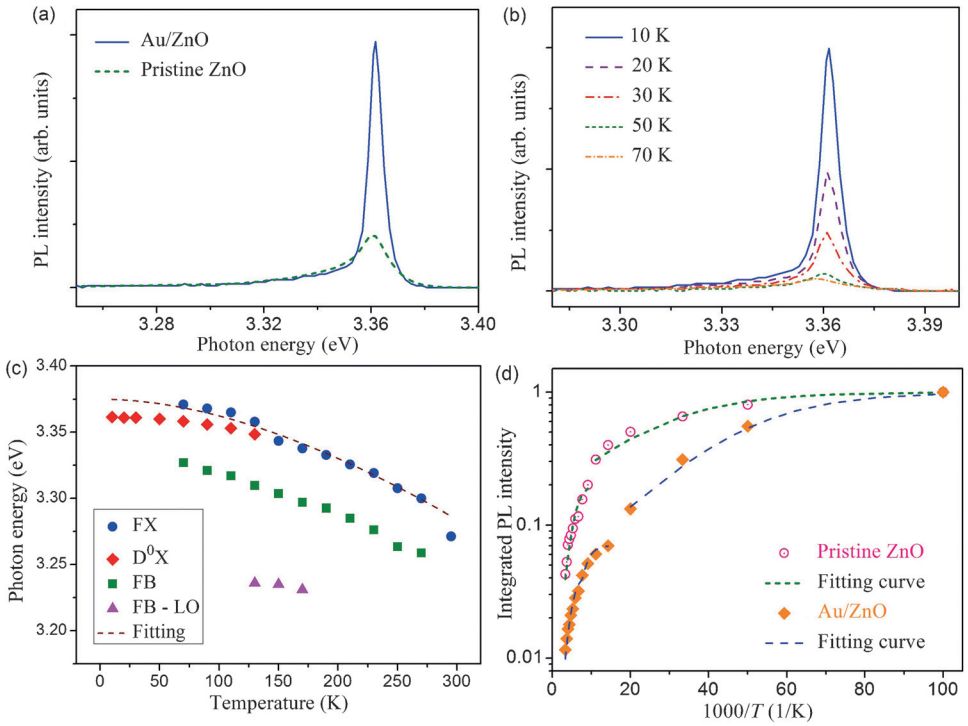

Figure 7. a) The NBE emissions of pristine ZnO NRs and Au/ZnO at the temperature of 10 K. b) The temperature dependent PL spectra of the Au/ZnO. c) The emission energy of the PL peaks as a function of temperature for the Au/ZnO. The FX data is fitted with Varshni's formula, as indicated by the dashed line. d) The integrated PL intensity as a function of inverse temperature of the Au/ZnO sample, in which the circles and diamonds denote the experimental data and the dashed lines represent the fitting results to Equation (9).

peak at 3.361 eV is attributed to the neutral-donor-bound-exciton emission (D^0X). The temperature-dependent PL of the Au/ZnO sample is shown in Figure 7b, in which a quick thermal quenching is revealed. As an analysis example, the PL spectrum of the Au/ZnO sample taken at 70 K was shown with Gaussian fits in Figure S3, Supporting Information. Three contributions can be resolved here: free exciton emission peak (FX), neutral-donor-bound-exciton emission, and free-to-bound emission (FB).

Figure 7c summarizes the temperature-dependence of emission peaks. In the low-temperature regime, the D^0X has the dominant contribution. Due to the thermal dissociation of bound excitons with increasing temperature, the FX emission eventually becomes the dominant PL emission in the high-temperature regime. With the increase of temperature, the emission peaks have a clear redshift due to the shrinkage of the intrinsic band gap. The temperature dependence of the FX can be fitted by the following empirical expression.

$$E(T) = E(0) - (\alpha T^2)/(\beta + T) \quad (8)$$

in which $E(0)$ is the transition energy of the free exciton at zero temperature and α and β are fitting parameters referred to as Varshni coefficients. The fitting results, which are denoted by the dashed line in Figure 7c, yield $E(0) = 3.375$ eV, $\alpha = 1.02$ meV K^{-1}, and $\beta = 710$ K. The calculated coefficients are consistent with reported values.[40,50,51] The Arrhenius plots of the integrated PL intensity as a function of reciprocal temperature for both samples are displayed in Figure 7d. The temperature-dependent activated behavior is given by:

$$I(T) = I_0/[1 + P\exp(-E_a/k_BT)] \quad (9)$$

in which $I(T)$ is the integrated PL intensity at T K, I_0 is a scaling factor, P is a process rate parameter, and E_a is the activation energy. The dashed lines in Figure 7d are the least-square fits of data with Equation (9). The fitted values for both samples are presented in Table 1. In the low-temperature regime, both samples have an activation energy of 5.7 meV even though their activated behaviors seem to differ to some degree. The process rate parameter of the Au/ZnO sample is higher than that of pristine ZnO NRs, which may reflect the drastic plasmonic enhancement effect described previously. In the high-temperature regime, the activation is governed by FX. Their activation energies are very close and the process rate parameters are also similar, as shown in Table 1.

Table 1. Calculated values for activation energies and process rate parameters.

Temperature region	Sample	E_a	P
low temperature	pristine ZnO NRs	5.7	4.7
low temperature	Au/ZnO	5.7	23.7
high temperature	pristine ZnO NRs	62	45
high temperature	Au/ZnO	59	50

Reusability of the Au/ZnO substrate

In the applications of liquid–solid heterogeneous catalytic processes and optoelectronics, reusability and durability are among the usual main concerns. For example, catalytic nanomaterials in powder form suffer from the problem of serious agglomeration due to high surface energy, so it poses a difficulty in the ease of application. In terms of catalyst recycling, the ZnO NRs array substrate provides a better option. The Au/ZnO NRs arrays deposited on the substrate are usually not prone to agglomeration at room temperature as they adhere firmly to the substrate and can take full advantage of the nanosized effect. In addition, the NRs array substrate can easily be separated from solution and then be recycled by using simple washing with deionized (DI) water and absolute ethanol with or without UV-light exposure. As shown in Figure 8a, several cycling runs in the photocatalytic degradation of MB over the Au/ZnO nanohybrids under UV-light illumination were carried out. In addition, photodegradation has been examined with the substrate after 60 days as well. The reaction time was limited to 120 min for each case. It is found that the Au/ZnO photocatalyst suffered a rather small loss of photodegradation efficiency even after four cycles and it was consistently stable during the photocatalytic oxidation of the pollutant molecules. From Figure 8b, the percentages of MB photodegradation are 91, 88, 87, and 85% for the first, second, third, and fourth

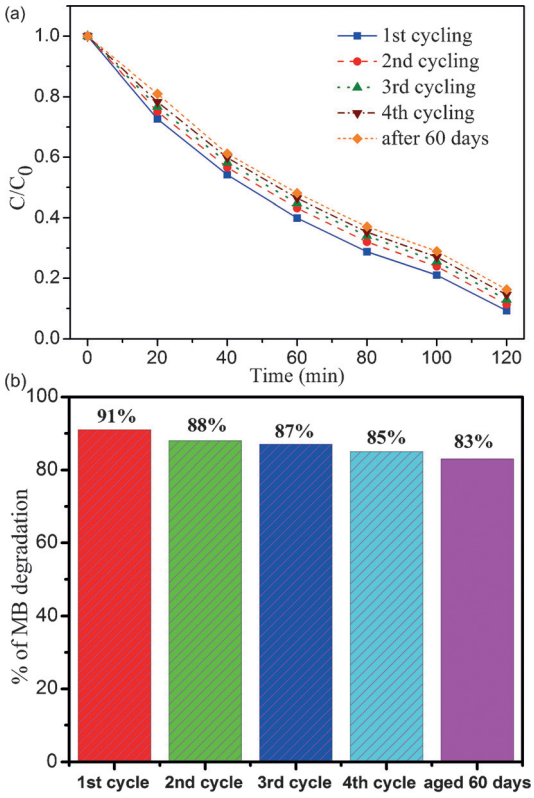

Figure 8. The reusability and durability tests of the Au/ZnO in four consecutive cycles and for aged 60 days: a) photocatalytic degradation profiles of MB over Au/ZnO catalyst b) percentages of MB degradation in the reuse of the photocatalyst.

cycle, respectively. Significant degradation of MB around 83% can be retained even with a 60 days aged substrate.

Figure 9a presents the PL of the substrate before and after cleaning the surface. The additional broad emission in blue region after photocatalytic experiment is due to the adsorbed MB or its degraded product. To remove the adsorbed dye or other pollutant, we cleaned the substrate with ethanol several times and immersed it into DI water and kept it for 10 min inside photoreactor with UV-light exposure. Then the substrate was collected and rinsed with DI water, and dried for further experiment. Cycling runs of PL tests were performed to understand the stability and durability, as shown in Figure 9b. Only NBE appears as before in the PL spectra and there is no extra defect or MB-related signal observed. The integrated NBE emission intensity, as shown in the inset of Figure 9b, only shows a small decline of 12% after 60 days. So it shows a good reliability and stability toward cycling usage. Finally, the XRD and SEM results after the fourth-cycle photocatalytic experiment were presented in Figure S4, Supporting Information. XRD pattern and SEM image both show similar characteristics with those from as-prepared sample, indicating there is no structural degradation of the catalyst even after the fourth-cycle photocatalytic experiment runs. Therefore, it is found that our Au/ZnO NR array substrate is stable enough to act as an efficient, recyclable, and bifunctional material platform.

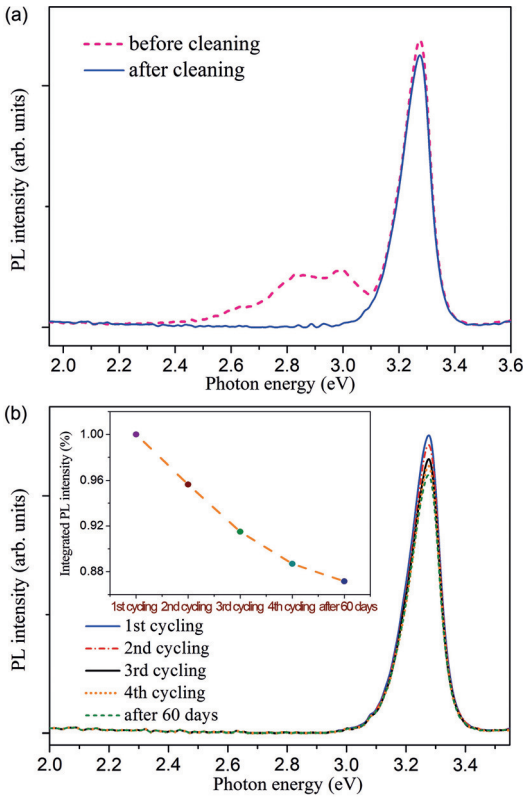

Figure 9. a) PL spectra of the substrate before and after cleaning the surface. b) PL spectra taken for consecutive four degradation/cleaning cycles and aged for 60 days. Inset: the integrated NBE emission intensity for the cycling runs.

Conclusions

In summary, we demonstrated the reusable and bifunctional Au/ZnO plasmonic platform, which possesses both enhanced UV/Vis photocatalysis and efficient emission properties by using a facile, economic, and green synthesis strategy. The enhancement of UV photodegradation is attributed to the charge separation within the nanocomposite and the strong-field enhancement in the vicinity of Au NPs, while the improved photodegradation in the visible region originates from the LSPR effect of Au NPs. Contrary to the usual cases that good NBE emission has to be sacrificed for an enhanced photocatalytic performance, we show that plasmonic-enhanced PL can still be retained in our system, which hints at the significance of the local-field enhancement effect. Mechanisms for the enhanced PL are discussed on the basis of local-field enhancement and electron-transfer model. A second-order Raman feature was revealed by a plasmonic-enhanced Raman scattering effect. The recyclability test of photocatalytic activity and emission efficiency showed that our Au/ZnO substrate remained stable and efficient after the fourth cycle and even for longer times. The present study provides a novel bifunctional platform with possible extended applications in recyclable UV/Vis energy-conversion, UV-emitting/detecting, and multifunctional/integrated devices.

Experimental Section

Materials

All the chemicals were of analytical grade and were purchased from Alfa Aesar and Merck Chemical Reagent, USA. Zinc nitrate hexahydrate ($Zn(NO_3)_2{\cdot}6H_2O$), hexamethylenetetramine (HMTA), chloroauric acid ($HAuCl_4$), zinc acetate dihydrate ($C_4H_{10}O_6Zn$, 99%), monoethanolamine (99%), isopropyl alcohol, and methyl blue were used as received without further purification.

Preparation of the ZnO nanorods

In the beginning, the ITO glass substrates ($1.5\times1.5\ cm^2$) were cleaned through sonication in a mixture of acetone and isopropyl alcohol (1:1), followed by cleaning with deionized water and subsequent drying under a N_2 atmosphere before use. The growth of the ZnO nanorods (NRs) starts from the preparation of ZnO seed layers. The substrate was spin-coated with an equimolar (0.05 M) ethanol solution of zinc acetate dehydrate and monoethanol amine. It was immediately annealed at 350 °C for 40 min to form the seed layer. Then, this ZnO-seeded substrate was immersed vertically into an equimolar (0.1 M) aqueous solution of zinc nitrate hexahydrate and HMTA in a Teflon autoclave. The hydrothermal growth of ZnO NRs was carried out in an oven at 90 °C for 10 h.

Preparation of the Au/ZnO hybrids

Au NPs were deposited on the ZnO NRs surface by a photochemical reaction. The as-grown ZnO NRs substrate was vertically placed into aqueous $HAuCl_4$ solution (1×10^{-4} M) and then exposed to UV light (256 nm) for 10 min. Finally, the substrate was cleaned by acetone and deionized water, and was then dried at 60 °C.

Characterization of pristine ZnO NRs and Au/ZnO hybrids

The morphology of as-obtained nanocomposite was studied by SEM (JEOL, SEM −6330) with an incident energy 200 keV. The structural information of the Au/ZnO nanocomposite was studied by XRD (Philips, X-Pert MRD) by using CuK_α radiation ($\lambda =$ 0.154 nm). The chemical bonding of the nanocomposite was analyzed using XPS (JEOL, JAMP-9500F). The optical absorption spectra were obtained using a UV/Vis spectrometer (JASCO, V-630). PL measurements were carried out by directing a chopped He-Cd laser beam to irradiate on the sample. The PL signal was collected and dispersed by a Jobin–Yvon Triax 550 monochromator equipped with a Hamamatsu R928 photomultiplier tube. A closed-cycle optical cryostat was used for low-temperature measurements. Room temperature Raman measurements were performed in a backscattering configuration on a micro-Raman setup equipped with Jobin–Yvon spectrometer iHR320 and a multichannel TE-cooled CCD detector. Raman measurements were performed with a red light laser (633 nm) and scattering geometry $z(xx+xy)z$.

Photocatalytic activity evaluation of Au/ZnO hybrids

To evaluate the photocatalytic activities of pristine ZnO NRs and Au/ZnO hybrids, MB ($C_{16}H_{18}N_3SCl$) was employed to play the role of a pollutant. The as-prepared ZnO NRs and Au/ZnO hybrid substrate of the same exposed area (1.5×1.5 cm^2) were placed inside a cylindrical quartz tube which was filled with 10 mL of aqueous MB solution (10 mg in 1 L DI water). The solution was first placed in the dark for 30 min before illumination to reach the adsorption–desorption equilibrium. The photocatalytic performance at RT was analyzed by measuring the MB absorption at $\lambda = 663$ nm using a UV/Vis spectrophotometer for a total duration of 2 h. A metal halide lamp (500 W) and UV lamp (256 nm) were adopted for visible and UV light sources, respectively. After each 20 min time interval, the illumination was stopped and MB solution was taken to a quartz cuvette for absorbance measurement. The solution was then brought back to the cylindrical quartz tube and the illumination started again for succeeded measurement. The efficiency of dye degradation can be calculated using the following equation:

$$\%\,\text{degradation} = (A_0 - A_t)/A_0 \times 100\,\% \qquad (10)$$

in which A_0 is the initial absorbance and A_t denotes the absorbance at time instant t.

Acknowledgements

This work was supported by the Ministry of Science and Technology of the Republic of China under grant No: MOST 104-2112-M-110-005.

Keywords: electron transfer · photocatalysis · photoluminescence · Raman spectroscopy · surface plasmon resonance

[1] J. Becker, K. R. Raghupathi, S. P. Jordan, K. Dan, T. Ranjit, *J. Phys. Chem. C* **2011**, *115*, 13844 – 13850.
[2] J. Schneider, M. Matsuoka, M. Takeuchi, J. Zhang, Y. Horiuchi, M. Anpo, D. W. Bahnemann, *Chem. Rev.* **2014**, *114*, 9919 – 9986.
[3] W. Peng, L. Han, Z. Wang, *Chem. Eur. J.* **2014**, *20*, 8483.
[4] W.-J. Chen, J.-K. Wu, J.-C. Lin, S.-T. Lo, H.-D. Lin, D.-R. Hang, M. F. Shih, C.-T. Liang, Y. H. Chang, *Nanoscale Res. Lett.* **2013**, *8*, 313.
[5] A. Z. Sadek, W. Wlodarski, Y. X. Li, W. Yu, X. Li, X. Yu, K. Kalantar-zadeh, *Thin Solid Films* **2007**, *515*, 8705 – 8708.
[6] J. L. Campbell, M. Breedon, K. Latham, K. Kalantar-zadeh, *Langmuir* **2008**, *24*, 5091 – 5098.
[7] J. Tang, J. R. Durrant, D. R. Klug, *J. Am. Chem. Soc.* **2008**, *130*, 13885 – 13891.
[8] T. Wang, R. Lv, P. Zhang, C. Li, J. Gong, *Nanoscale* **2015**, *7*, 77 – 81.
[9] G. Colón, M. C. Hidalgo, J. A. Navío, E. Pulido Melián, O. González Díaz, J. M. Doña Rodríguez, *Appl. Catal. B* **2008**, *83*, 30.
[10] S. K. Kansal, M. Singh, D. Sud, *J. Hazard. Mater.* **2007**, *141*, 581.
[11] L. Zhu, M. Hong, G. W. Ho, *Sci. Rep.* **2015**, *5*, 11609.
[12] M. T. Qamar, M. Aslam, I. M. I. Ismail, N. Salah, A. Hameed, *ACS Appl. Mater. Interfaces* **2015**, *7*, 8757 – 8769.
[13] Q. Wang, B. Geng, S. Wang, *Environ. Sci. Technol.* **2009**, *43*, 8968 – 8973.
[14] L. Sun, D. Zhao, Z. Song, C. Shan, Z. Zhang, B. Li, D. Shen, *J. Colloid Interface Sci.* **2011**, *363*, 175 – 181.
[15] Y. Chen, D. Zeng, K. Zhang, A. Lu, L. Wang, D.-L. Peng, *Nanoscale* **2014**, *6*, 874.
[16] M. Wu, W.-J. Chen, Y.-H. Shen, F.-Z. Huang, C.-H. Li, S.-K. Li, *ACS Appl. Mater. Interfaces* **2014**, *6*, 15052 – 15060.
[17] X. Li, Y. Zhang, X. Ren, *Opt. Express* **2009**, *17*, 8735.
[18] C. W. Cheng, E. J. Sie, B. Liu, C. H. A. Huan, T. C. Sum, H. D. Sun, H. J. Fan, *Appl. Phys. Lett.* **2010**, *96*, 071107.
[19] S. T. Kochuveedu, J. H. Oh, Y. R. Do, D. H. Kim, *Chem. Eur. J.* **2012**, *18*, 7467.
[20] R. Udayabhaskar, B. Karthikeyan, P. Sreekanth, R. Philip, *RSC Adv.* **2015**, *5*, 13590 – 13597.
[21] S. G. Zhang, X. W. Zhang, Z. G. Yin, J. X. Wang, J. J. Dong, H. L. Gao, F. T. Si, S. S. Sun, Y. Tao, *Appl. Phys. Lett.* **2011**, *99*, 181116.
[22] K. W. Liu, Y. D. Tang, C. X. Cong, T. C. Sum, A. C. H. Huan, Z. X. Shen, L. Wang, F. Y. Jiang, X. W. Sun, H. D. Sun, *Appl. Phys. Lett.* **2009**, *94*, 151102.
[23] K. Wu, Y. Lu, H. He, J. Huang, B. Zhao, Z. Ye, *J. Appl. Phys.* **2011**, *110*, 023510.
[24] M. M. Brewster, X. Zhou, M.-Y. Lu, S. Gradečak, *Nanoscale* **2012**, *4*, 1455 – 1462.
[25] a) X. D. Zhou, X. H. Xiao, J. X. Xu, G. X. Cai, F. Ren, C. Z. Jiang, *Europhys. Lett.* **2011**, *93*, 57009; b) Y. J. Fang, J. Sha, Z. L. Wang, Y. T. Wan, W. W. Xia, Y. W. Wang, *Appl. Phys. Lett.* **2011**, *98*, 033103.
[26] R. Viter, Z. Balevicius, A. A. Chaaya, I. Baleviciute, S. Tumenas, L. Mikoliunaite, A. Ramanavicius, Z. Gertnere, A. Zalesska, V. Vataman, V. Smyntyna, D. Erts, P. Miele, M. Bechelany, *J. Mater. Chem. C* **2015**, *3*, 6815 – 6821.
[27] M. Ahmad, S. Yingying, A. Nisar, H. Sun, W. Shen, M. Weie, J. Zhu, *J. Mater. Chem.* **2011**, *21*, 7723.
[28] T. Rakshit, S. P. Mondal, I. Manna, S. K. Ray, *ACS Appl. Mater. Interfaces* **2012**, *4*, 6085 – 6095.
[29] L. K. Ono, B. R. Cuenya, *J. Phys. Chem. C* **2008**, *112*, 4676 – 4686.
[30] T. Wang, B. Jin, Z. Jiao, G. Lu, J. Ye, Y. Bi, *J. Mater. Chem. A* **2014**, *2*, 15553 – 15559.
[31] T. H. Yang, L. D. Huang, Y. W. Harn, C. C. Lin, J. K. Chang, C. I. Wu, J. M. Wu, *Small* **2013**, *9*, 3169 – 3182.
[32] J. Zhang, X. Liu, S. Wu, B. Cao, S. Zheng, *Sens. Actuators B* **2012**, *169*, 61 – 66.
[33] M. R. Khan, T. W. Chuan, A. Yousuf, M. N. K. Chowdhury, C. K. Cheng, *Catal. Sci. Technol.* **2015**, *5*, 2522 – 2531.
[34] C. S. Turchi, D. F. Ollis, *J. Catal.* **1990**, *122*, 178 – 192.
[35] Z. Sun, C. Wang, J. Yang, B. Zhao, J. R. Lombardi, *J. Phys. Chem. C* **2008**, *112*, 6093 – 6098.
[36] D.-R. Hang, K. H. Sharma, S. E. Islam, C. Chen, M. M. C. Chou, *Appl. Phys. Express* **2014**, *7*, 041101.
[37] S. Kuriakose, B. Satpati, S. Mohapatra, *Phys. Chem. Chem. Phys.* **2014**, *16*, 12741 – 12749.
[38] S. J. Chen, Y. C. Liu, Y. M. Lu, J. Y. Zhang, D. Z. Shen, X. W. Fan, *J. Cryst. Growth* **2006**, *289*, 55.
[39] Y. M. Hu, C. Y. Wang, S. S. Lee, T. C. Han, W. Y. Chou, G. J. Chen, *J. Raman Spectrosc.* **2011**, *42*, 434 – 437.
[40] D.-R. Hang, S. E. Islam, K. H. Sharma, S.-W. Kuo, C.-Z. Zhang, J.-J. Wang, *Nanoscale Res. Lett.* **2014**, *9*, 632.
[41] R. Cuscó, E. Alarcón-Lladó, J. Ibáñez, L. Artús, J. Jiménez, B. Wang, M. J. Callahan, *Phys. Rev. B* **2007**, *75*, 165202.

[42] J. Zhao, X. Yan, Y. Yang, Y. Huang, Y. Zhang, *Mater. Lett.* **2010**, *64*, 569 – 572.
[43] Y. Dong, C. Feng, P. Jiang, G. Wang, K. Li, H. Miao, *RSC Adv.* **2014**, *4*, 7340 – 7346.
[44] M. K. Lee, T. G. Kim, W. Kim, Y. M. Sung, *J. Phys. Chem. C* **2008**, *112*, 10079 – 10082.
[45] Y. Matsumoto, R. Kanemoto, T. Itoh, S. Nakanishi, M. Ishikawa, V. Biju, *J. Phys. Chem. C* **2008**, *112*, 1345 – 1350.
[46] J.-C. Bian, F. Yang, Z. Li, J.-L. Zeng, X.-W. Zhang, Z.-D. Chen, J. Z. Y. Tan, R.-Q. Peng, H.-Y. He, J. Wang, *Appl. Surf. Sci.* **2012**, *258*, 8548 – 8551.
[47] B. Lamprecht, J. R. Krenn, G. Schider, H. Ditlbacher, M. Salerno, N. Felidj, A. Leitner, F. R. Aussenegg, *Appl. Phys. B* **2001**, *79*, 51.
[48] J. Li, H. C. Ong, *Appl. Phys. Lett.* **2008**, *92*, 121107.
[49] M. Liu, M. Pelton, P. Guyot-Sionnest, *Phys. Rev. B* **2009**, *79*, 035418.
[50] K. Saravanan, B. K. Panigrahi, R. Krishnan, K. G. M. Nair, *J. Appl. Phys.* **2013**, *113*, 033512.
[51] D.-R. Hang, S. E. Islam, K. H. Sharma, C. Chen, C.-T. Liang, M. M. C. Chou, *Semicond. Sci. Technol.* **2014**, *29*, 085004.

Received: May 31, 2016
Published online on August 31, 2016